Computational dosimetry in MRI in presence of hip, knee or shoulder implants: do we need accurate surgery models?

IOP Publishing Phys. Med. Biol. 67 (2022) 245022 https://doi.org/10.1088/1361-6560/aca5e6

Physics in Medicine & Biology

IPEM Institute of Physics and Engineering in Medicine

OPEN ACCESS

RECEIVED
28 May 2022

REVISED
10 November 2022

ACCEPTED FOR PUBLICATION
24 November 2022

PUBLISHED
15 December 2022

PAPER

Computational dosimetry in MRI in presence of hip, knee or shoulder implants: do we need accurate surgery models?

Alessandro Arduino[1], **Fabio Baruffaldi**[2], **Oriano Bottauscio**[1,*], **Mario Chiampi**[1], **Jessica A Martinez**[1], **Umberto Zanovello**[1] and **Luca Zilberti**[1]

[1] Istituto Nazionale di Ricerca Metrologica (INRIM), Torino, Italy
[2] IRCCS Istituto Ortopedico Rizzoli, Bologna, Italy
[*] Author to whom any correspondence should be addressed.

E-mail: o.bottauscio@inrim.it

Keywords: MRI safety, implants, *in silico* trials

Supplementary material for this article is available online

Abstract

Objective. To quantify the effects of different levels of realism in the description of the anatomy around hip, knee or shoulder implants when simulating, numerically, radiofrequency and gradient-induced heating in magnetic resonance imaging. This quantification is needed to define how precise the digital human model modified with the implant should be to get realistic dosimetric assessments. *Approach.* The analysis is based on a large number of numerical simulations where four 'levels of realism' have been adopted in modelling human bodies carrying orthopaedic implants. *Main results.* Results show that the quantification of the heating due to switched gradient fields does not strictly require a detailed local anatomical description when preparing the digital human model carrying an implant. In this case, a simple overlapping of the implant CAD with the body anatomy is sufficient to provide a quite good and conservative estimation of the heating. On the contrary, the evaluation of the electromagnetic field distribution and heating caused by the radiofrequency field requires an accurate description of the tissues around the prosthesis. *Significance.* The results of this paper provide hints for selecting the 'level of realism' in the definition of the anatomical models with embedded passive implants when performing simulations that should reproduce, as closely as possible, the *in vivo* scenarios of patients carrying orthopaedic implants.

1. Introduction

In silico studies are becoming a consolidated paradigm in many sectors of biomedicine, including pharmaceuticals and chemicals, as a need to develop robust and reliable methods to reduce or replace animal testing (Madden *et al* 2020).

In general, computer simulation of humans is found to be a powerful tool in biomedical research, allowing systematic investigations that are not always possible *in vivo*. This trend has also involved the verification of the safety and efficacy of medical technologies, to the point that regulatory agencies recently started receiving and accepting evidence obtained *in silico*, i.e. through modelling and simulation, to the request for marketing authorization of new medical products (Viceconti *et al* 2021).

To this purpose, in the last decade, there has been an extraordinary evolution of digital human models suitable for different applications, from biomechanics (El-Bojairami *et al* 2020) to bioelectromagnetics (Gosselin *et al* 2014), enabling a large adoption of numerical simulations to investigate the impact of external physical agents on the human body and complementing experimental studies.

In the specific area of magnetic resonance imaging (MRI), computational dosimetry is becoming an essential tool to support safety evaluation, especially because of the extension of ultrahigh field scanners in clinics and the scanning of patients carrying implants. In particular, this latter issue has acquired great relevance due to the increasing number of patients with implanted devices (OECD/EU 2016) and the growing use of MRI for a wide

range of diagnostic questions. A recent review article has analysed the status of the research in this field and the open issues (Winter *et al* 2021).

The assessment of MRI safety in presence of patients carrying implants requires the availability of reliable and validated tools, capable of reproducing as close as possible the *in vivo* scenarios. *In silico* simulations have become a natural procedure for standardisation (ISO_TS_10974_2018(E)), and their adoption will likely increase to support further development of the testing methods.

Previous studies have evaluated the effects of the 'level of realism' in the adopted digital human models on the analysis of MRI RF induced heating. They focused on body models without implants, evaluating the effects of model complexities, model truncation and clustering of tissue types to reduce their number (Wolf *et al* 2013, Fiedler *et al* 2018).

Analogously, the importance of describing realistic details of the implant-tissues-field interaction is highlighted in many studies of MRI safety. A wide literature is available for active implantable medical devices (AIMDs), as the concern of scanning these devices has emerged earlier. For instance, some studies show how the pacemaker lead trajectory can significantly modify the amount of heating (Nordbeck *et al* 2009, Mattei *et al* 2008, 2010, Yao *et al* 2021, Nguyen *et al* 2022). Similar analyses were performed on Deep Brain Stimulation (DBS) devices, analysing the role of lead configuration (Golestanirad *et al* 2017, McElcheran *et al* 2019), the accurate modelling of the electrodes (Guerin *et al* 2018), body's composition and the tissue around electrodes (Iacono *et al* 2013, Bhusal *et al* 2021) and the way to reduce the heating (McElcheran *et al* 2015). The need for high-resolution, whole body models embedding AIMDs was addressed by Jeong *et al* (2021). Radiofrequency (RF) heating induced by coronary stents was also largely addressed in the literature (see for example Santoro *et al* (2012)).

More recently, greater attention to the modelling of the interaction between MRI fields and passive implants (e.g. orthopaedic devices) has grown as a consequence of the evidence of heating effects due to RF and switched gradient fields. An extensive analysis of the effect of the relative position of hip implants with respect to RF coil was published by Powell *et al* (2012), at 1.5 T and 3 T. The heating due to RF field in a realistic hip implant model was studied by (Seo and Wang 2021) considering a homogeneous phantom. Specific attention to the tissues around the hip prosthesis was addressed in the modelling analysis by Destruel *et al* (2019), where the male model Duke from the Virtual Population (ViP) was modified to include hip prostheses; the heads of the femurs were replaced with muscle tissue to simulate a bilateral total hip arthroplasty and bone tissue was added in the pelvis to ensure a tight fit of the acetabular component. The hip implant heating due to the superposition of radiofrequency and switched-gradient fields was addressed by Arduino *et al* (2021), paying attention to the role of the spatial distribution of the gradient field and the characteristics of the MRI sequence. Other contributions related to passive implants are those of Bassen and Zaidi (2022) and Song *et al* (2018). Nonetheless, to the authors' knowledge, no previous work has analysed the influence of the level of detail to realistically simulate the operation for inserting the implant, despite the fact that the use of virtual surgeries has allowed a considerable improvement in the success of operations for a joint replacement (Chen *et al* 2001).

This work intends to investigate and quantify the role of detailed surgery models in predicting the heating caused by the interaction of massive orthopaedic implants with RF and switched gradient fields. This is aimed to answer the question: 'Are accurate surgery models really needed in MRI computational dosimetry?'. The problem has been investigated using two highly detailed anatomical models, the 26 year-old female Yoon-Sun and the 84 year old male Glenn, both belonging to the Virtual Population (ViP) (Sim4Life). The primary focus has been given to hip replacements, but knee and shoulder replacements were also analysed. In all cases, realistic (not generic) digital implant models were analysed, with sizes compatible with the anatomy of the two human models. During the virtual surgery, special care was paid to shape the periprosthetic bones of the human model to optimally fit the relevant implants. In this operation, a section of the bones was replaced by the implant and another section was cut away and replaced by filling tissues. Implant position, type, and size were double-checked by orthopaedic surgeons specialised in joint replacement surgery.

Two main exposure scenarios were investigated in the simulations: the heating caused by a low-pass birdcage RF coil at 1.5 T and a high-pass birdcage RF coil at 3 T, and the heating due to a switched field generated by the gradient coils (GCs) of a tubular scanner, considering an EPI and a TrueFISP pulse sequences.

The phenomenon was investigated in terms of temperature increase in the tissues after an exposure of 900 s. Results with different versions of the anatomical model are compared, from the simplest case where homogeneous tissue properties are adopted (electric and thermal properties of the gel prescribed by ASTM F2182 (ASTM F2182-19e2 2019)), to the case, largely adopted in literature, of insertion of the implant by CAD overlapping, to the final configuration obtained by accurate virtual surgery. In this latter case, due to the possible variability of the tissues filling the gaps around the implant, two extreme cases were considered, filling them either with connective tissue or synovial fluid.

A large number of simulations were performed for GC-heating, including two anatomical models of different size and weight, with the aim of considering in the analysis implants of different size, taking into

account that this parameter has a significant role in the power deposition within metallic components (Wooldridge *et al* 2021). For RF-heating, the same two anatomical models were compared but limiting the attention to the case of the hip, which is the largely diffused orthopaedic implant and to corroborate the results. The analysis of the role of an accurate surgery model on RF heating is then extended also to two other implants (knee and shoulder), but limiting the attention to one anatomical model.

2. Materials and methods

2.1. Considered levels of details around the implanted prosthesis

Due to the different physical mechanisms involved, the analysis was performed separately for RF and GC. For each kind of prosthesis and considered anatomical model (Glenn or Yoon-Sun), four levels of detail around the implanted device (denoted in the following as surgery 0, 1, 2A and 2B) were investigated and compared for the same anatomical position:

- Surgery 0: homogeneous anatomical model consisting of a single compartment following the external geometry of the body. The model was filled with a homogeneous medium with the properties indicated in the ASTM standard (see table 1); the implant CAD models were superposed in the proper anatomical positions;
- Surgery 1: a heterogeneous anatomical model with implants overlapped to the native tissues, without realistic local modifications of the original anatomy, simply assigning a higher priority to the prostheses. This arrangement corresponds to the conditions adopted in most of the published results of simulations with implants.
- Surgery 2A: anatomical model with realistic modification of the tissues surrounding the implant. For this arrangement, a virtual surgery was performed, and the connective tissue was used as a filler in the area surrounding the surgery (see table 1).
- Surgery 2B: anatomical model with realistic modification of the tissues surrounding the implant. The anatomy was the same as in Surgery 2A, but the synovial fluid was used as a filler in the area surrounding the surgery. The electric properties of the cerebrospinal fluid from the IT'IS Foundation database are assigned to the synovial fluid (Hasgall *et al* 2018), because of their thermal properties similarity (Moghadam *et al* 2015).

2.2. Anatomical model selection

The most appropriate ViP models were chosen according to the best match of the population with the different categories and sizes of considered implants. In particular, Yoon-Sun (adult female, 26 years old, height equal to 152 cm, BMI 23.6 kg m^{-2}) and Glenn (adult male, 84 years old, height equal to 173 cm, BMI equal to 20 kg m^{-2}) models were selected to the purpose. The high-resolution anatomical models were used, from ViP Version 3, with a spatial resolution of 0.5 mm $\times$ 0.5 mm $\times$ 0.5 mm.

2.3. Implants selection

Orthopaedic implants selection was based on the prevalence analysis of the population with the different types of replacement. Hip and knee arthroplasties are the most applied orthopaedic surgical procedures in the EU, while shoulder arthroplasty represents about one-tenth of the previous (OECD/EU 2016).

Due to their prevalence and considering the related heating risk for patients undergoing MRI examinations, hip implants are analysed extensively in this paper (both GC and RF simulations are performed on Glenn and Yoon-Sun models). For knee and shoulder implants, GC results are reported for both anatomical models (to evidence the role of implant size), whereas RF results are reported only for the Yoon-Sun model. For the hip and knee implants, the same commercial products were adopted with two sizes depending on the anatomy (Yoon-Sun or Glenn). For the shoulder implant, two different commercial products were selected (Shoulder #1 and Shoulder #2 for Yoon-Sun and Glenn, respectively) for the best fit into the anatomical models.

2.3.1. Hip implant

A total hip prosthesis, uncemented, with metal-on-polyethylene coupling was considered. The stem (model Apta-Fix, manufactured by Adler Ortho® SpA, Italy, www.adlerortho.com) was made in titanium alloy with a coating of hydroxyapatite, with a length of 125 mm (or 140 mm for Glenn). The spherical head of the stem was made in CrCoMo alloy, with a diameter of 28 mm (or 32 mm). The acetabular cup (model Fixa Ti-Por, manufactured by Adler Ortho® SpA, Italy, www.adlerortho.com) was made in titanium alloy, having a diameter

Table 1. The physical properties of the ASTM gel, connective tissue, synovial fluid, muscle, bone and implant materials. For the bone, a range is reported including the property values relevant to bone cancellous, cortical, bone marrow red and bone marrow yellow. (*) In the RF simulations, the metallic components of the implants are handled using Perfectly Electric Conductors (PEC) conditions. (*n/a*) The value of the electrical conductivity and relative permittivity of tissues is not relevant for GC simulations, where the power deposition takes place only in the metallic objects.

	Electric conductivity S m^{-1}			Relative permittivity			Perfusion coefficient W/(m^3 K)	Thermal conductivity W/(m K)	Specific heat capacity J/(kg K)	Mass density kg m^{-3}
	GC	RF-1.5 T	RF-3 T	GC	RF-1.5 T	RF-3 T				
ASTM gel	*n/a*	0.470	0.470	n/a	80.0	80.0	0	0.54	4152	998
Connective tissue	*n/a*	0.474	0.499	n/a	59.5	51.9	2096	0.47	3432	1142
Synovial fluid	*n/a*	2.070	2.140	n/a	97.3	84.0	0	0.57	4095	1007
Muscle	*n/a*	0.688	0.719	n/a	72.2	73.5	2553	0.49	3421	1090
Bone	*n/a*	(0.022 ÷ 0.160)	(0.024 ÷ 0.180)	n/a	(7.21 ÷ 30.90)	(6.23 ÷ 26.30)	(1208 ÷ 8793)	(0.19 ÷ 0.32)	(1313 ÷ 2666)	(980 ÷ 1908)
Titanium Alloy		0.580 10^6 (*)			0 (*)		0	7.20	520	4420
CrCoMo		1.160 10^6 (*)			0 (*)		0	14.00	450	8445
UHMWPE		1.777			0		0	0.66	4915	1007

of 42 mm (or 54 mm) and a shell thickness of 3.5 mm (or 5 mm), with an Ultra High Molecular Weight Polyethylene (UHMWPE) insert having an internal diameter of 28 mm (or 32 mm).

2.3.2. Knee implant

A total knee prosthesis (model Genus MB, manufactured by Adler Ortho® SpA, Italy, www.adlerortho.com), uncemented version, was considered. The femoral component was made of CrCoMo alloy of maximum size of 66 mm (or 77 mm). The tibial component was made of titanium alloy with a maximum size 66 mm (or 77 mm). An UHMWPE insert was present having a thickness of 17 mm (or 16 mm).

2.3.3. Shoulder implant #1

For the Yoon-Sun model, an anatomic shoulder hemi-prosthesis (model SMR Anatomic, manufactured by LimaCorporate SpA, Italy, https://limacorporate.com/), uncemented, was considered. The humeral stem was made of titanium alloy, with a length of 105 mm, while the hemispherical humeral head was made of CrCoMo alloy, having a diameter of 40 mm.

2.3.4. Shoulder implant #2

For the Glenn model, a reverse shoulder prosthesis (model SMR Reverse, manufactured by LimaCorporate SpA, Italy), uncemented, was considered. The humeral stem was made of titanium alloy, with a length of 115 mm, while the humeral cup was made of CrCoMo alloy, having a diameter of 40 mm. An UHMWPE glenosphere of diameter 40 mm was present.

CAD models of the hip and knee implants were provided by the manufacturer, while CAD models of the shoulder implants were obtained from the 3D scanning of the physical objects.

2.4. Procedures for implant positioning within the body

Sim4Life V5.2 (ZMT, Zurich MedTech, Switzerland) was used to import the selected Computer Aided Design (CAD) models, and to virtually implant them into the selected anatomical models along the pre-defined clinical routings suggested by the surgeon experience. Virtual implants were applied on one side, modifying the original tissues of the human models when required to properly accommodate the specific implant. Implant position, type and size were double-checked by orthopaedic surgeons specialised in joint replacement surgery. In the preparation of the models with level of detail Surgery 2, special care was made to shape the periprosthetic bones of the human model to optimally fit the relevant implants. This generally translated into removing part of the bones that were replaced by the implant itself and by filling tissues. A total number of six surgical procedures were simulated, by the combination of three types of implants and two anatomical models. The modified models are shown in figure 1(A).

In figure 1(B), the three levels of approximations are evidenced by showing a section of the Yoon-Sun body model in correspondence of each considered implant. It is evident how, in the Surgery 2, parts of the bones have been removed after the insertion of the implant (red material) and the voids have been replaced by the filler material (in yellow).

2.5. MRI systems

A low-pass and a high-pass birdcage body coils were considered for transmission at 1.5 T (64 MHz) and 3 T (128 MHz) respectively. Typical 16-leg body coils (diameter: 713 mm, height: 450 mm) were considered, including a cylindrical shield (diameter: 752 mm, height: 1500 mm). Coil conductors and shields were simulated as Perfect Electric Conductors (PEC). The coils were tuned to the respective Larmor frequencies deploying the ASTM phantom as a reference load. The coils were supplied by means of two 90° spaced ports in standard circular polarisation mode.

A full body gradient coil set for tubular MRI scanners (Solaris-R by Nanjing Cichen) was used. It is composed of three axial coils, which constitute the x, y, and z gradient coils used in clinical scanners. The overall length was 1.5 m, and the internal diameter was 720 mm. For each coil, a virtual model was generated. The sensitivity constants of GCs were 56.1 μT/(mA) for the X and Y coils and 57.8 μT/(mA) for the Z coil.

2.6. GC sequences

Starting from the results obtained by Arduino *et al* (2021), the simulations were restricted here to the exposure of the worst-case in terms of heating, which occur when using the EPI (Echo-Planar Imaging) and TrueFISP (True Fast Imaging with Steady State Precession) sequences. Parameters of the considered sequences are collected in table 2 and the sequence waveforms are reported in Figures. S1 and S2. For EPI sequence, three cases were considered, assuming the frequency encoding along each of the three axes (EPI-X, EPI-Y, EPI-Z)

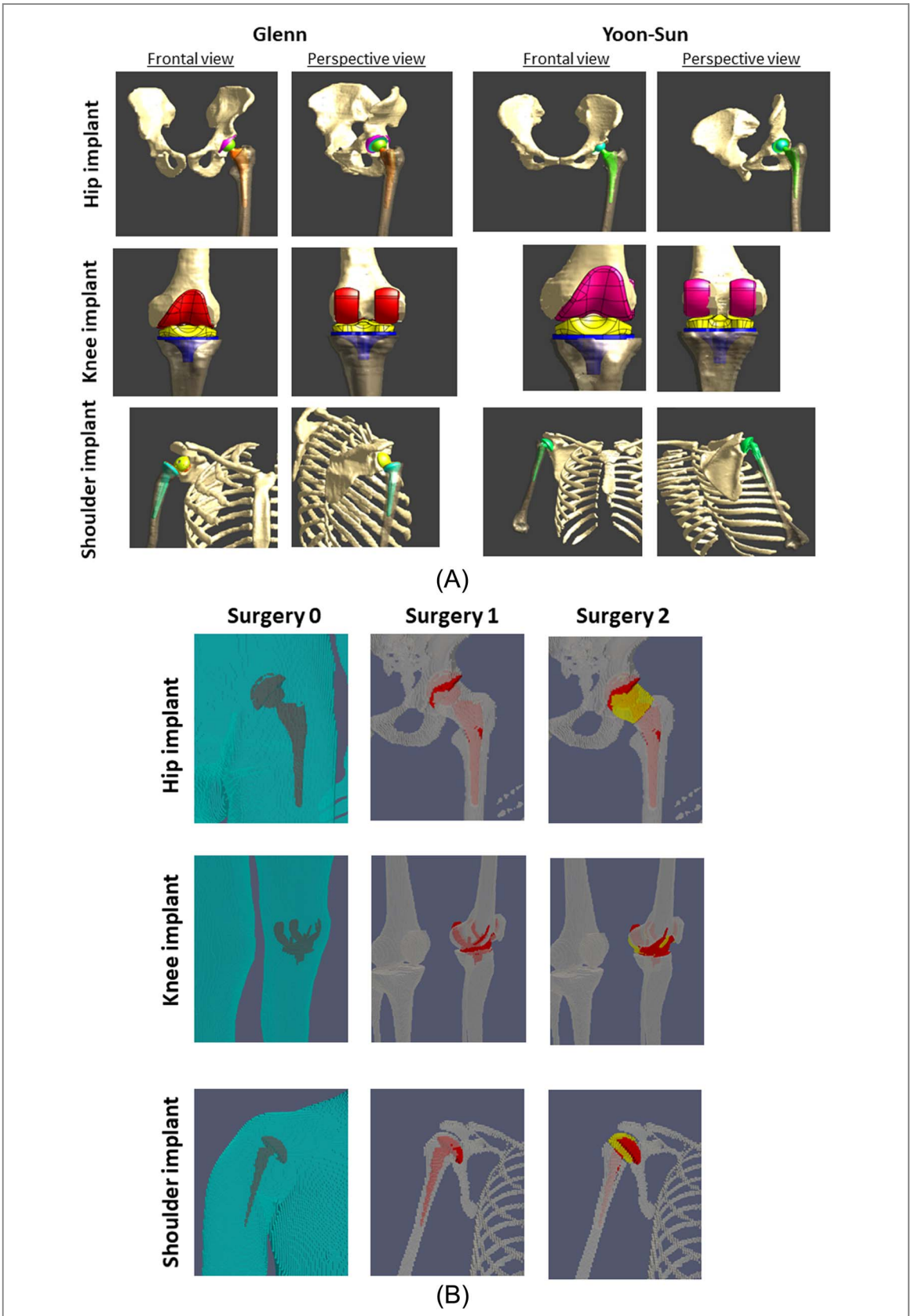

Figure 1. (A) Glenn and Yoon-Sun anatomical models with the three considered prostheses (hip, knee and shoulder). (B) Anatomical body model Yoon-Sun with the details of the three considered surgeries for each implant. The red material represents the implant, whereas the yellow one in Surgery 2 is the adopted filler material, where parts of the bones have been removed after the insertion of the implant.

Table 2. Sequence parameters.

	Flip angle	RF pulse duration	Time-BW product	TE	TR	Readout BW	Max slew rate	Matrix dimension	FOV
EPI	90°	1.6 ms	4	21 ms	43 ms	150 kHz	167 T m^{-1} s^{-1}	64 × 64	182 mm × 182 mm
TrueFISP	45°	1 ms	4	3.2 ms	6.4 ms	126.3 kHz	200 T m^{-1} s^{-1}	256 × 256	120 mm × 180 mm

2.7. GC simulations

GC Simulations were performed for both Yoon-Sun and Glenn models, for all the considered implants, taking into account that GC heating is mainly affected by the implant size. Preliminary investigations showed that a mesh size of 2 mm was adequate to achieve stable results. Nine body positions within the MRI bore were considered, from femur/knee imaging to head imaging, as shown in figure S3 for the Yoon-Sun model.

For the Yoon-Sun model, four sequences were considered: EPI-X, EPI-Y, EPI-Z and TrueFISP. For the Glenn model, the analysis was restricted to the EPI-Z sequence only. For each case, the temperature increase after 900 s of exposure was recorded for each voxel.

Simulations were performed in two steps, following the computational scheme discussed in Arduino *et al* (2019). The implementation of the electromagnetic problem complies with the one described in Bottauscio *et al* (2015). The analysis was restricted to the region of the metallic implant where power deposition occurs, repeating the simulation for each harmonic component of the GC signal. The related energy density due to the superposition of all harmonics was then computed in each voxel.

Thermal simulations were carried out on the whole body by solving the Pennes' bioheat equation expressed in terms of temperature elevation (Arduino *et al* 2017). A finite difference method (FDM) homemade software was used, applying a Douglas–Gunn (DG) time split scheme implemented on graphics processing units (GPUs). Simulations were performed on Intel Xeon CPU E5-2680 v2, 128 GB RAM, with NVIDIA K80 GPU card.

2.8. RF simulations

Considering the implants models previously mentioned, RF simulations for the Glenn and Yoon-Sun models with hip implants were performed at 1.5 T and 3 T. For all the conditions, the coil input power was adjusted to generate an average B_1^+ of 2 μT on a 2D transverse slice at the coil isocenter. The metallic components of the implants were simulated as Perfectly Electric Conductors (PEC), which, at RF, guarantees accurate results in terms of power deposition (Zilberti *et al* 2021).

The virtual model was placed in three positions within the birdcage coil, corresponding to the placement of the implant in the coil centre (ISO) and at the coil lower and upper extremities (MINUS and PLUS), which correspond to the positions where the maximum power deposition and consequent temperature increase are usually found (Powell *et al* 2012, Arduino *et al* 2021). An example is shown in figure S4 for the hip implant.

The commercial software Sim4Life V5.2 (Sim4Life) was used to solve the RF electromagnetic and the transient thermal problem to calculate the distributions of SAR and the temperature increase within the body. The electromagnetic problem was solved in the entire human body by a finite difference time domain (FDTD) solver applied on an unstructured mesh with a minimum step equal to about 0.5 mm.

Using Sim4Life, the thermal problem (Pennes' bioheat equation) was solved according to an FDTD method with homogeneous Dirichlet boundary conditions. Sim4Life ran on a workstation with an Intel Xeon CPU E5-2650 v2 @ 2.60 GHz and a GPU NVIDIA Tesla K20c.

To ensure that the analysis was performed by looking at the most significant local power deposition due to the presence of the implant and the consequent heating in the surrounding tissues, a region of analysis was selected assuming a shaped shell around each specific implant, having a 30 mm thickness (see figure S4). In this region, the maximum temperature increase ΔT after 900 s and the local SAR values averaged on 2 g and 10 g were recorded.

3. Results

In the following sections, GC and RF heating are analysed separately. This is justified by the results found in Arduino *et al* (2021), where it was demonstrated that, under realistic conditions, the simultaneous occurrence of RF and GC thermal heating does not sensibly modify the maximum temperature increase in tissues, due to the different spatial distribution of the two thermal effects.

3.1. GC-heating

The majority of the results are reported for the EPI-Z sequence, comparing the two anatomical models. Figure 2 shows, as an example, the effect of the surgery model on the time evolution of the maximum temperature increase on the surface of the hip implant for the Yoon-Sun model. A similar behaviour is found with the Glenn model, considering that the heat dissipation is limited within the implant at these frequencies.

Figure 3 summarises the maximum temperature increase after 900 s with EPI-Z, for the different body positions and levels of detail. In the Yoon-Sun model, the maximum temperature increases are found in positions Pos9, Pos7 and Pos4 for the hip, knee and shoulder implants, respectively. The maximum temperature increases are similar for the models with Surgery 2A and 2B (hip: 0.79 °C, knee: 0.77 °C, shoulder: 0.97 °C). The

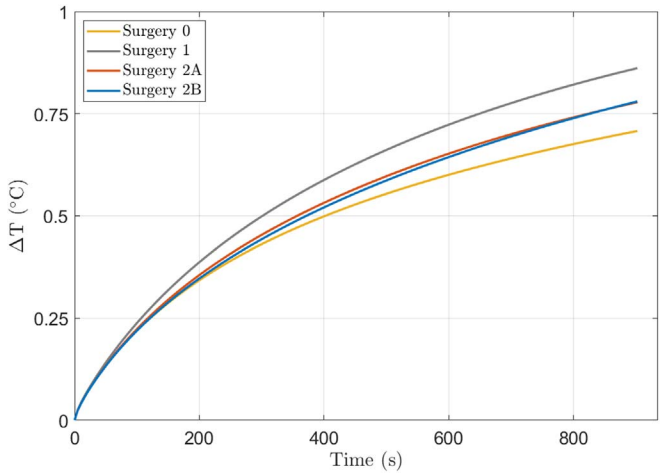

Figure 2. GC heating consequent to an EPI-Z sequence: time evolution of the maximum temperature increase on the hip implant surface for the Yoon-Sun model in the body position which gives rise to the maximum heating (Pos3).

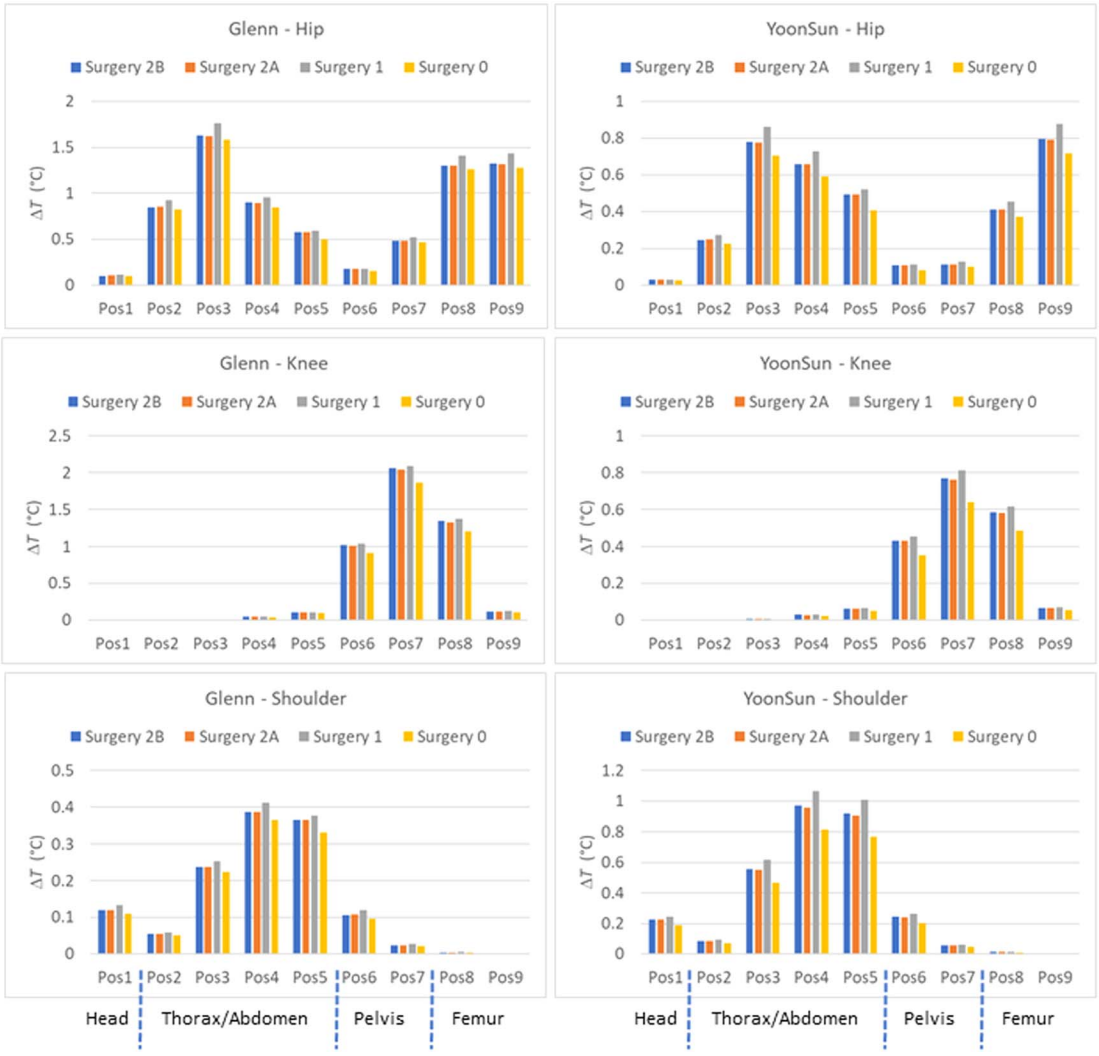

Figure 3. Maximum temperature increases after 900 s of exposure to GC fields for each considered position of the body within the MRI bore. Simulations with Glenn model (left plots) and Yoon-Sun model (right plots) from Pos1 (head imaging) to Pos9 (Femur/Knee imaging). Results refer to the EPI-Z sequence with frequency encoding along the *z*-axis.

Table 3. Maximum GC temperature increase (°C) within the body (considering all body positions) after 900 s of exposure for the Yoon-Sun model and the four considered gradient sequences.

Implant	Sequence	Surgery 0	Surgery 1	Surgery 2A	Surgery 2B
Hip	EPI-X	0.807	1.011	0.968	0.969
	EPI-Y	1.184	1.570	1.512	1.515
	EPI-Z	0.718	0.878	0.791	0.794
	FISP	0.430	0.539	0.500	0.500
Knee	EPI-X	0.160	0.206	0.193	0.194
	EPI-Y	0.459	0.637	0.589	0.588
	EPI-Z	0.638	0.811	0.762	0.771
	FISP	0.217	0.282	0.264	0.266
Shoulder	EPI-X	1.162	1.493	1.380	1.403
	EPI-Y	0.467	0.608	0.557	0.565
	EPI-Z	0.817	1.066	0.955	0.972
	FISP	0.555	0.735	0.669	0.677

larger temperature increases are obtained with Surgery 1 (hip: 0.88 °C, knee: 0.81 °C, shoulder: 1.1 °C), whereas the lower temperature increases are found with Surgery 0 (hip: 0.72 °C, knee: 0.64 °C, shoulder: 0.82 °C).

The maximum temperature increase in the Glenn model moves to position Pos3 for the hip implant, whereas the positions of maximum stress remain unchanged for the knee and shoulder implants. As in the simulations involving the Yoon-Sun model, the maximum temperature increases are similar for the two models with virtual Surgery 2A and 2B (hip: 1.6 °C, knee: 2.1 °C, shoulder: 0.39 °C). Some differences have been found in Surgery 0 (hip: 1.6 °C, knee: 1.9 °C, shoulder: 0.36 °C) and Surgery 1 (hip: 1.77 °C, knee: 2.1 °C, shoulder: 0.41 °C).

In both the human models and for all the implant types, Surgery 0 and Surgery 1 always show the lowest and the highest values of the temperature increases, respectively. Moreover, the ratio between the heating estimated in Surgery 1 and in a more realistic scenario (Surgery 2) was found to be almost independent of the considered anatomical model and implant type (∼1.08 for Yoon-Sun and ∼1.06 for Glenn).

The comparison between different implants shows that, in Glenn anatomy, the knee and hip give rise to the highest temperature values, whereas in the shoulder implant, the values significantly decrease, due to the presence in this implant of a significant non-metallic component (glenosphere). In the Yoon-Sun model, whose shoulder implant is fully metallic, the magnitude of the temperature increase is approximately the same for all implants, with the maximum peak reached in the shoulder. However, due to the smaller size, the temperature increases for hip and knee are significantly lower with respect to the Glenn model.

The spatial distributions of the heating around the implant are presented in figure S5 showing maps of the temperature increase in a vertical section of the body for Yoon-Sun and Glenn models. The comparison of the maps puts in evidence the differences among the four considered levels of detail of the model.

The summary of the results obtained with all four considered sequences, restricted to the Yoon-Sun model, is reported in table 3. All these results confirm that Surgery 1 always gives rise to the highest values, heating in Surgery 0 is always the lowest, and results obtained with Surgery 2A and 2B are quite close to each other.

3.2. RF-heating

The use of different surgery models and the implant position with respect to the birdcage RF coil (MINUS, ISO or PLUS) impact RF-heating. Figure 4 shows the time evolution of the temperature increase for Yoon-Sun and Glenn models with the hip implant at 3 T. The results show how the time evolution is affected by the combination of body position and surgery model. As opposed to GC-heating, the temperature increase for the Surgery 0 (homogeneous medium) is sensibly lower, despite in same cases this configuration shows the maximum value of the 2g-SAR. This can be explained by the higher values of specific heat capacity of the ASTM gel. This latter also affects the time evolution of the temperature in case of Surgery 0, which has an almost adiabatic behaviour in the considered time interval.

The spatial distribution of the temperature increase after 900 s, the 2g-SAR and 10g-SAR around the implant are plotted in figures 5 and 6, respectively for Yoon-Sun and Glenn models with hip implants at 1.5 T and 3 T. For each considered coil position (MINUS, ISO and PLUS), the slice in which the maximum temperature occurred and the corresponding 2g-SAR and 10g-SAR are shown. Similar plots are reported for the Yoon-Sun model with knee and shoulder implants, respectively in figures 7 and 8.

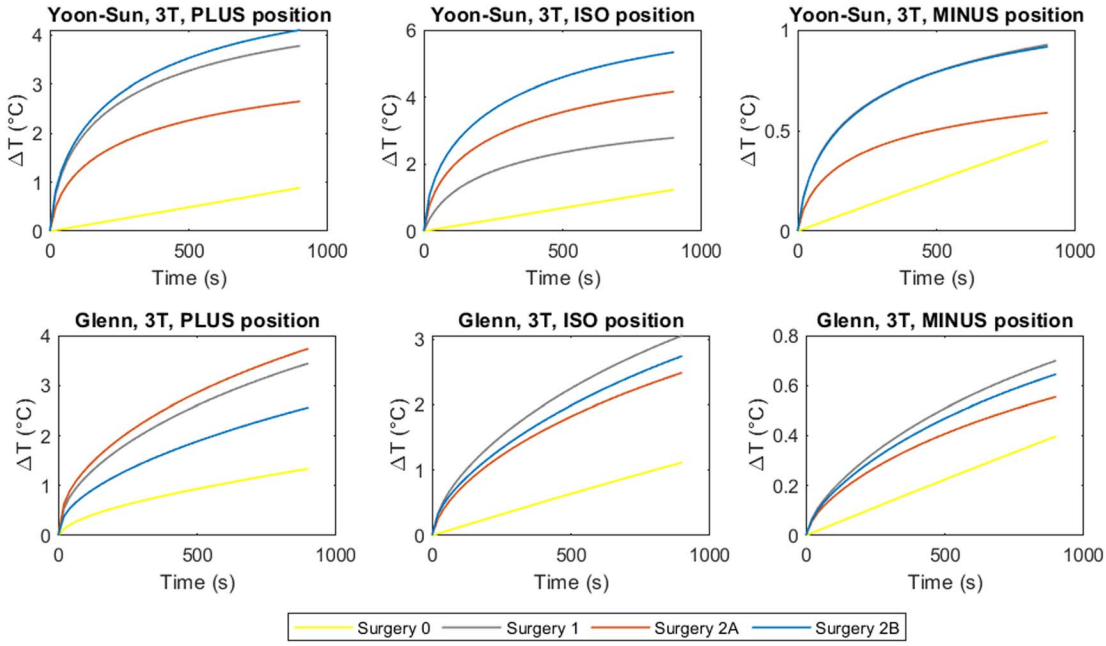

Figure 4. RF heating for Yoon-Sun (upper plots) and Glenn (lower plots) models with hip implant at 3 T: time evolution of the maximum temperature increase on the hip implant surface for three body positions (PLUS, ISO and MINUS) obtained with the different levels of surgery models.

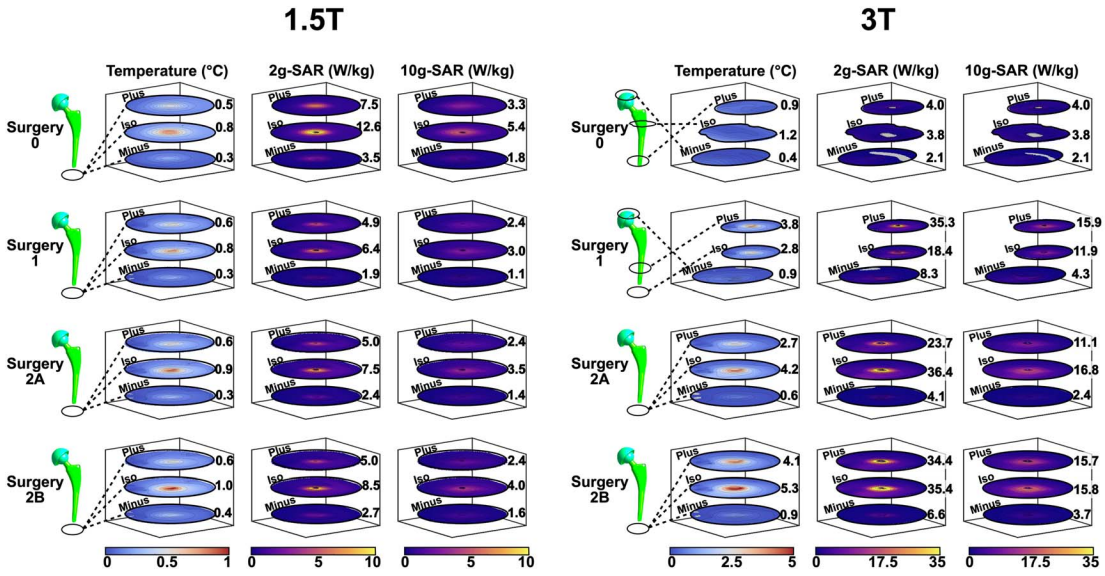

Figure 5. Maps of the temperature increase after 900 s, 2-g SAR, and 10 g SAR in body slices close to the implant. For each body position (MINUS, ISO and PLUS) the slice refers to the spatial point where the maximum temperature increase after 900 s is found. Results refer to Yoon-Sun model with hip implant under 1.5 and 3 T field strengths.

For the hip implant, the maximum temperature increase ΔT, the 2g-SAR, and 10g-SAR values for the different coil positions at 1.5 T and 3 T are summarised in tables 4 and 5 respectively. The reported 2g-SAR and 10g-SAR were evaluated in the same location where the maximum heating occurred. The results show the effect that the different surgery models have on temperature increase. Overall, SAR and temperature were greater at 3 T compared to 1.5 T.

For the Yoon-Sun model with hip implant, the maximum temperature increase at 1.5 T is found in the ISO position with Surgery 2B (1.0 °C), whereas for the same position Surgery 2A gives 0.89 °C and Surgery 1 0.76 °C. The temperature increases for the MINUS position are the lowest, whereas intermediate values are found for the PLUS position. In all cases, Surgery 2B gives rise to the maximum temperature increase (0.35 °C for MINUS,

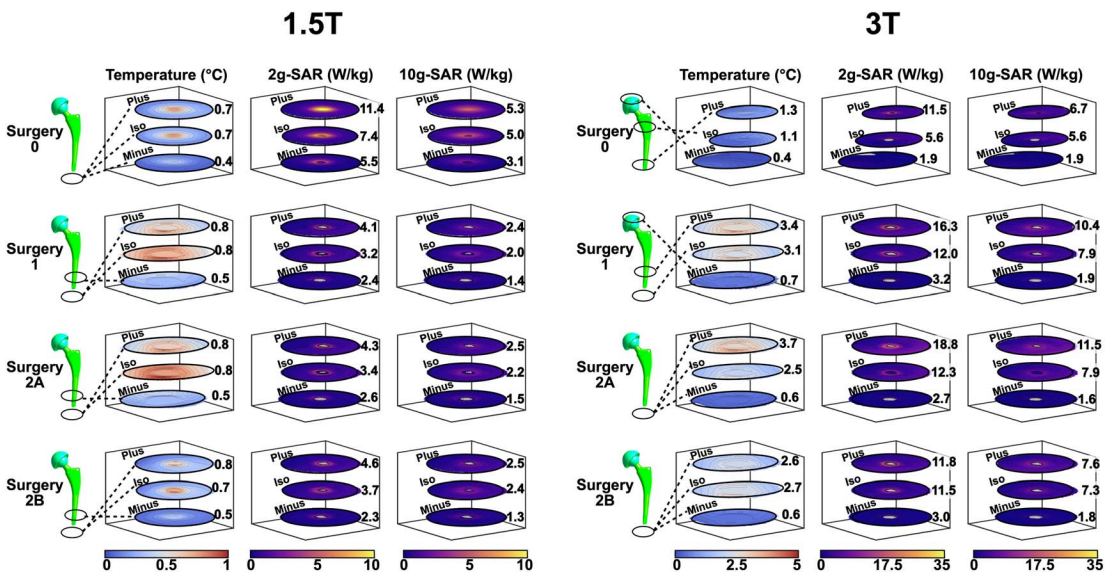

Figure 6. Maps of the temperature increase after 900 s, 2-g SAR, and 10 g SAR in body slices close to the implant. For each body position (MINUS, ISO and PLUS) the slice refers to the spatial point where the maximum temperature increase after 900 s is found. Results refer to Glenn model with hip implant under 1.5 and 3 T field strengths.

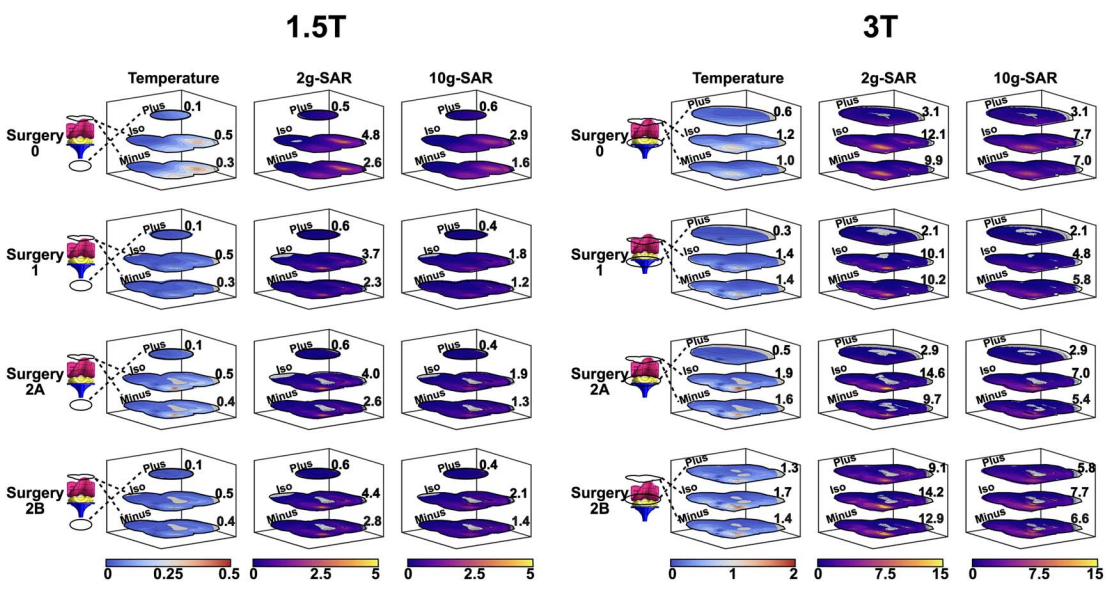

Figure 7. Maps of the temperature increase after 900 s, 2-g SAR, and 10 g SAR in body slices close to the implant. For each body position (MINUS, ISO and PLUS) the slice refers to the spatial point where the maximum temperature increase after 900 s is found. Results refer to Yoon-Sun model with knee implant under 1.5 and 3 T field strengths.

0.62 °C for PLUS and 1.0 °C for ISO). On the contrary, Surgery 0 almost always resulted in the minimum temperature increase (0.28 °C for MINUS, 0.48 °C for PLUS and 0.79 °C for ISO).

The Yoon-Sun model with the hip implant, however, exhibits a distinct behaviour at 3 T, where Surgery 2B resulted in maximum temperature values for PLUS and ISO positions (4.10 °C and 5.34 °C), whereas for MINUS position the maximum is found for Surgery 1 (0.93 °C). For all positions, Surgery 0 resulted in the lowest ΔT (0.89 °C for PLUS, 1.24 °C for ISO and 0.45 °C for MINUS).

For the Glenn model with hip implant, at 1.5 T the highest temperature increase is found for Surgery 2A in the PLUS position (0.84 °C). For the same position, temperature for Surgery 2B was 0.81 °C and for Surgery 1 it was 0.79 °C. The minimum heating is found for the MINUS positions, with the temperature increase ranging from 0.43 °C (Surgery 0) to 0.46 °C (Surgery 2B).

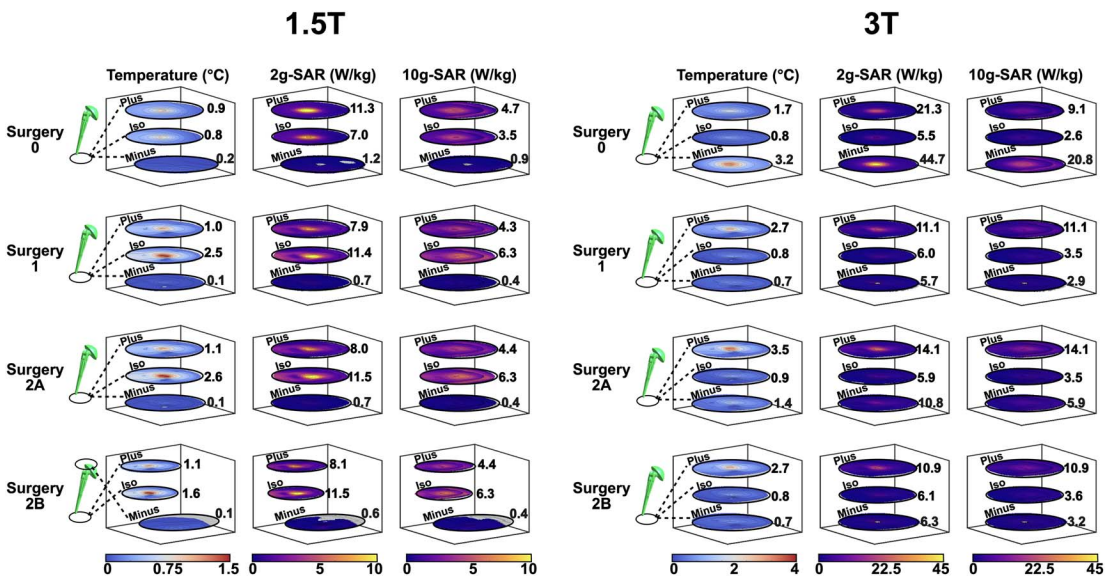

Figure 8. Maps of the temperature increase after 900 s, 2 g SAR, and 10 g SAR in body slices close to the implant. For each body position (MINUS, ISO and PLUS) the slice refers to the spatial point where the maximum temperature increase after 900 s is found. Results refer to Yoon-Sun model with shoulder implant under 1.5 and 3 T field strengths.

At 3 T the maximum heating in the Glenn model with hip implant was observed in the ISO position with Surgery 1 (3.06 °C), followed by Surgery 2B (2.74 °C) and Surgery 2A (2.49 °C). Similarly to the Yoon-Sun model, Surgery 0 resulted in the lowest temperature increase (1.12 °C).

Similar comparisons, for the knee and the shoulder implants implanted in the Yoon-Sun model, are reported in tables 6 and 7 respectively. For the knee implant, the maximum heating is found in the ISO position both at 1.5 T (0.6 °C) and at 3 T (4.16 °C). At 1.5 T, the temperature increases are almost identical between Surgery 0, Surgery 1, Surgery 2A and Surgery 2B. On the contrary, at 3 T a larger difference is found between surgeries, moving from 1.36 °C (Surgery 1) to 1.95 °C (Surgery 2A) for the knee implant, and from 2.73 °C (Surgery 1) to 3.47 °C (Surgery 2A) for the shoulder implant.

For this latter, the maximum heating is found in correspondence of the ISO position at 1.5 T (1.57 °C) and of the PLUS position at 3 T (3.47 °C). At 1.5 T, the temperature increases are almost identical for all considered levels of detail, apart from Surgery 0 which either underestimates (PLUS and ISO) or overestimates (MINUS) the temperature increase. On the contrary, at 3 T a large difference is found moving from the Surgery 2A (3.47 °C) to the Surgery 1 (2.73 °C), with Surgery 2A showing the maximum values for all positions. For the shoulder implant, Surgery 0 either underestimates or overestimates the results.

4. Discussion

4.1. GC-heating

The overall GC-induced heating is mainly determined by the size and the shape of the implant. Therefore, the analysis has been carried on considering two anatomical models with implants of different sizes. Indeed, when the same commercial implant (hip and knee) is considered, the GC-induced heating is lower in the Yoon-Sun model than the one obtained for the Glenn model, which involves implants with larger components (e.g. the acetabular cup and ball for the hip implant), with a consequent higher power deposition in the metallic parts.

Differences in the GC-induced heating estimated with the different surgery models depend exclusively on the thermal properties of the biological tissues, because the electromagnetic power is deposited only within the metallic components of the implant and the low conductive native tissues do not alter it. With respect to the other versions of the model, Surgery 0 (homogenous body) always underestimates the temperature increase despite the lack of blood perfusion, because the thermal conductivity of the gel is considerably higher than that of bones (the main tissue in the proximity of the implant).

On the other hand, Surgery 1 always gives rise to the largest temperature increase, probably because, in this case, the implant is surrounded mainly by the bone, which acts as a thermal insulator and prevents the heat dissipation from the implant to the tissues.

Surgery 2 provides intermediate results, which are weakly affected by the selected filling material. Indeed, the maximum temperature increases estimated with Surgery 2A and with Surgery 2B are almost identical. This

Table 4. Results for hip implant at 1.5 T: maximum temperature increase after 900 s in the region of analysis around the implant and related 2g-SAR and 10g-SAR. For each position, the maximum temperature increase ΔT, 2g-SAR and 10g-SAR are highlighted in bold character, excluding Surgery 0. The (*) character highlights, for each body position, the absolute maximum value of 2g-SAR, including Surgery 0.

		PLUS				ISO				MINUS			
		Surgery 0	Surgery 1	Surgery 2A	Surgery 2B	Surgery 0	Surgery 1	Surgery 2A	Surgery 2B	Surgery 0	Surgery 1	Surgery 2A	Surgery 2B
Yoon-Sun	ΔT (°C)	0.48	0.61	0.61	0.62	0.79	0.76	0.89	1.00	0.28	0.25	0.30	0.35
	2g-SAR (W kg^{-1})	7.53 (*)	4.92	4.99	5.00	12.6 (*)	6.39	7.46	8.45	3.52 (*)	1.92	2.35	2.73
	10g-SAR (W kg^{-1})	3.27	2.38	2.41	2.41	5.42	3.02	3.51	3.95	1.84	1.12	1.36	1.57
Glenn	ΔT (°C)	0.69	0.79	0.84	0.81	0.66	0.75	0.80	0.73	0.43	0.45	0.45	0.46
	2g-SAR (W kg^{-1})	11.4 (*)	4.09	4.28	4.58	7.40 (*)	3.21	3.41	3.70	5.54 (*)	2.36	2.60	2.27
	-SAR (W kg^{-1})	5.39	2.42	2.54	2.72	5.03	2.04	2.17	2.44	3.10	1.40	1.54	1.33

Table 5. Results for hip implant at 3 T: maximum temperature increase after 900 s in the region of analysis around the implant and related 2g-SAR and 10g-SAR. For each position, the maximum temperature increase ΔT, 2g-SAR and 10g-SAR are highlighted in bold character, excluding Surgery 0. The (*) character highlights, for each body position, the absolute maximum value of 2g-SAR, including Surgery 0.

		PLUS				ISO				MINUS			
		Surgery 0	Surgery 1	Surgery 2A	Surgery 2B	Surgery 0	Surgery 1	Surgery 2A	Surgery 2B	Surgery 0	Surgery 1	Surgery 2A	Surgery 2B
Yoon-Sun	ΔT (°C)	0.89	3.78	2.65	4.10	1.24	2.79	4.17	5.34	0.45	0.93	0.59	0.92
	2g-SAR (W kg^{-1})	3.96	35.3 (*)	23.7	34.4	3.79	18.4	36.4 (*)	35.4	2.12	8.35 (*)	4.16	6.58
	10g-SAR (W kg^{-1})	3.96	15.9	11.1	15.7	3.80	11.9	16.9	15.8	2.11	4.35	2.37	3.71
Glenn	ΔT (°C)	1.34	3.44	3.74	2.56	1.12	3.06	2.49	2.74	0.40	0.70	0.55	0.64
	2g-SAR (W kg^{-1})	11.6	16.3	18.8 (*)	11.8	5.64	12.0	12.3 (*)	11.5	1.94	3.19 (*)	2.66	2.98
	10g-SAR (W kg^{-1})	6.74	10.4	11.5	7.61	5.64	7.89	7.93	7.31	1.93	1.93	1.62	1.79

Table 6. Results for knee implant at 1.5 T and 3 T: maximum temperature increase after 900 s in the region of analysis around the implant and related 2g-SAR and 10g-SAR. For each position, the maximum temperature increase ΔT, 2g-SAR and 10g-SAR are highlighted in bold character, excluding Surgery 0. The (*) character highlights, for each body position, the absolute maximum value of 2g-SAR, including Surgery 0.

		PLUS				ISO				MINUS			
		Surgery 0	Surgery 1	Surgery 2A	Surgery 2B	Surgery 0	Surgery 1	Surgery 2A	Surgery 2B	Surgery 0	Surgery 1	Surgery 2A	Surgery 2B
1.5 T	ΔT (°C)	0.10	0.08	0.08	0.09	0.48	0.51	0.56	0.60	0.27	0.32	0.35	0.38
	2g-SAR (W kg^{-1})	0.54	0.61	0.62	0.64 (*)	4.83 (*)	3.71	4.04	4.36	2.61	2.34	2.63	2.80 (*)
	10g-SAR (W kg^{-1})	0.54	0.39	0.40	0.41	2.91	1.80	1.94	2.07	1.59	1.18	1.30	1.37
3 T	ΔT (°C)	0.61	0.33	0.45	1.27	1.18	1.36	1.95	1.70	1.03	1.38	1.56	1.40
	2g-SAR (W kg^{-1})	3.09	2.12	2.85	9.06 (*)	12.1	10.1	14.6 (*)	14.2	9.91	10.2	9.75	12.9 (*)
	10g-SAR (W kg^{-1})	3.06	1.37	1.88	5.82	7.68	4.76	6.98	7.75	6.99	5.81	5.43	6.64

Table 7. Results for shoulder implant at 1.5 T and 3 T: maximum temperature increase after 900 s in the region of analysis around the implant and related 2g-SAR and 10g-SAR. For each position, the maximum temperature increase ΔT, 2g-SAR and 10g-SAR are highlighted in bold character, excluding Surgery 0. The (*) character highlights, for each body position, the absolute maximum value of 2g-SAR, including Surgery 0.

		PLUS				ISO				MINUS			
		Surgery 0	Surgery 1	Surgery 2A	Surgery 2B	Surgery 0	Surgery 1	Surgery 2A	Surgery 2B	Surgery 0	Surgery 1	Surgery 2A	Surgery 2B
1.5 T	ΔT (°C)	0.86	1.04	1.06	1.07	0.81	1.55	1.56	1.57	0.16	0.10	0.10	0.11
	2g-SAR (W kg^{-1})	11.3 (*)	7.88	8.03	8.09	6.99	11.4	11.5	11.5 (*)	1.24 (*)	0.74	0.75	0.59
	10g-SAR (W kg^{-1})	4.66	4.34	4.41	4.44	3.47	6.26	6.31	6.34	0.91	0.41	0.42	0.43
3 T	ΔT (°C)	1.71	2.73	3.47	2.73	0.77	0.83	0.92	0.85	3.17	0.68	1.43	0.75
	2g-SAR (W kg^{-1})	21.3	21.3	28.2 (*)	21.8	5.47	5.95	5.95	6.05 (*)	44.7 (*)	5.72	10.8	6.29
	10g-SAR (W kg^{-1})	9.08	11.1	14.1	10.9	2.63	3.49	3.46	3.57	20.8	2.95	5.86	3.25

happens for all the body positions (corresponding to different amounts of power dissipation) and for both the Yoon-Sun and Glenn models. The results obtained by simple overlapping (Surgery 1) always overcome the ones given by the most sophisticated surgery models (Surgery 2A and 2B), differing by less than 10 %.

This overall behaviour was found to be almost independent of the anatomical model, considered sequence and implant type. This result seems to lead to the belief that accurate surgery models are not strictly needed to obtain reliable results, considering that the impact of an accurate surgery is only limited to the heat thermal diffusion from the implant towards the surrounding tissues. This has a direct impact in the anatomical model assembling, because the implant can be simply overlapped to the native tissues, ensuring conservative results and in line with those obtained with a more evolved anatomical model. The only requirement is to check the reliability of the discretization of the metallic components to properly evaluate the power dissipation in the implant.

4.2. RF-heating

For the RF exposure, the analysed scenarios are those that usually provide the maximum heating (Powell *et al* 2012). The local distribution of tissues around the implant plays a more significant role with respect to the GC-induced heating, making it difficult to predict the behaviour of the different implants with the different levels of detail, also within the same anatomical human model. This evidence could be explained by the fact that, for RF-induced heating, both electric and thermal properties affect the entire process.

In almost all the analysed cases, the homogenous anatomical model (Surgery 0) shows the slowest temperature evolution with time and underestimates the temperature increase with respect to the most detailed surgeries. The discrepancies range from 20 % up to 80 % considering all the anatomical models and implants. This is probably due to the larger thermal conductivity and specific heat capacity of the ASTM gel with respect to the bones. In terms of power deposition, in Surgery 0, the averaged SAR (2g-SAR and 10g-SAR) are always overestimated at 1.5 T (up to around 100 %), while they are always underestimated at 3 T (up to around 90 %) with respect to the other versions of the surgery.

On the other hand, the distribution of temperature increase estimated with Surgeries 1, 2A and 2B correlates well with the corresponding distributions of average SAR, better with the 2g-SAR than with the 10g-SAR.

Based on the maximum temperature increase ΔT and 2g-SAR comparison between the most detailed surgery models (2A and 2B) and Surgery 1, the following conclusions can be drawn. At 1.5 T, for the Yoon-Sun model with hip implant the variations of the temperature increase and 2g-SAR are up to 40 % using the Surgery 2 models. Lower variations are found with the Glenn model, where they reach 20 %.

Variations between surgeries increase at 3 T, where the Yoon-Sun model with hip implant resulted in differences of up to 100 % for both temperature increase and 2g-SAR. This increase from 1.5 to 3 T did not appear for the Glenn model, where the discrepancies between Surgeries 1 and 2 were up to 20 %.

Lower differences between surgeries are found for the Yoon-Sun model with knee and shoulder implant at 1.5 T. In these cases, maximum variations are found up to 20 % for the knee implant and to 10 % for the shoulder implant.

On the contrary, higher variations are found at 3 T particularly for the knee implant (up to 400 % for both the temperature increase and the 2g-SAR for a given body position) and for the shoulder implant (up to 110 %).

As a general result, Surgery 1 always produces the lowest heating making reference to the worst scenario of exposure (body position), while the results of Surgery 0 deviate significantly from the other results. This is in line with the outcomes obtained in Fiedler *et al* (2018) for anatomical models in absence of implants.

Nonetheless, modifying the properties of the filling material from connective tissue (Surgery 2A) to synovial fluid (Surgery 2B) affects the computed SAR distribution less than moving from Surgery 1 to Surgery 2, suggesting that the height of the bone cut is the parameter driving the differences between the surgery models.

From these overall data, it is reasonable to conclude that the use of more accurate surgery models with orthopaedic implants has a non-negligible impact on the radiofrequency simulation results. This has a direct consequence on the process of simulating implant exposure to RF fields. From a researcher point of view, the main difference between the levels of detail of the virtual surgery is the effort required to prepare the models and the degrees of freedom (i.e. the properties of the replaced tissues) that have to be constrained in order to fully define the simulation setup. No impacts can be envisaged for the computational burden, since the use of accurate surgery models does not modify the discretization grid used in the electromagnetic and thermal solvers, leading to the same computational time and memory requirements.

5. Conclusions

From the above analysis, it results that GC-induced heating does not strictly need the adoption of advanced virtual surgery when building the digital human model equipped with implants. A simple overlapping of the

implant CAD with the body anatomy, respecting the realistic position of the implant with respect to the bones, is sufficient to provide a stable and conservative estimation of the heating.

Differently, for the RF-induced heating, the power deposition in tissues surrounding the implant is affected also by the electromagnetic properties of these materials. In this case, an accurate surgery model is found to be essential, because there is no simple rule to rescale the results obtained with one level of detail of the surgery model to those obtained with another one. This makes a critical task the requirement of the last ASTM F2182 revision to establish a relationship between the temperature increase for the implant tested in the gelled-saline filled phantom and that expected in the patient population.

Modifying the properties of the filling materials from connective tissue to synovial fluid has a noticeable impact on the maximum temperature increase only for RF-induced heating, while GC-induced heating remains unaffected. From an applicative point of view, the results presented here provide some hints about the geometrical and physical parameters that play a critical role for the realistic simulation of what happens *in vivo*. However, the results presented in this paper do not enable us to conclude that either proposed versions of Surgery 2 provide fully realistic descriptions, closer to the *in vivo* scenario, of a patient carrying an implant. Anyway, the analysis proves that the RF calculations in presence of large metallic implants are very sensitive to the local properties and distribution of the tissues around the implant. This comes with two consequences. The first one is that further work is surely needed to identify the most realistic way to simulate the exposure of a patient carrying orthopaedic implants. The second consequence is that, until no definite conclusions can be drawn, results of dosimetric RF simulations should be complemented with related uncertainty (or confidence interval), to take into account that such results exhibit the above-mentioned non-negligible sensitivity.

The general conclusions found in this paper for MRI heating, could be extended to other situations where orthopaedic metallic implants interact with electromagnetic fields, as in medical treatments (e.g. hyperthermia) or in presence of external sources (e.g. electric vehicle inductive charging systems). Depending on the characteristic of the electromagnetic field source, the power deposition can either be restricted to the implant volume, giving rise to behaviours more similar to the MRI GC-induced heating, or involve the tissues surrounding the implant, similarly to the MRI RF-induced heating. In the latter case, the need for accurate surgery models should be analysed for the specific scenario to draw reliable conclusions.

Acknowledgments

The results presented here have been developed in the framework of the 17IND01 MIMAS Project. This project has received funding from the EMPIR Programme, co-financed by the Participating States and from the European Union's Horizon 2020 Research and Innovation Programme.

Authors thank ZMT for making the modified versions of the ViP models, equipped with the considered orthopedic implants, available in the voxelized structure for subsequent *in silico* analysis.

CAD models of hip and knee implants were kindly provided by the manufacturer of prosthetic devices Adler Ortho® SpA, Italy (www.adlerortho.com).

Authors wish to thanks the orthopaedic surgeons F Giardina, E Tassinari (Orthopaedic-Traumatology and Prosthetic surgery and revisions of hip and knee implants, Istituto Ortopedico Rizzoli, Italy) and E Guerra (Shoulder and Elbow Surgery, Istituto Ortopedico Rizzoli, Italy) for supervising virtual surgery activities.

ORCID iDs

Alessandro Arduino https://orcid.org/0000-0002-4829-5130
Fabio Baruffaldi https://orcid.org/0000-0001-8784-5652
Oriano Bottauscio https://orcid.org/0000-0002-5437-4396
Mario Chiampi https://orcid.org/0000-0003-0049-3792
Jessica A Martinez https://orcid.org/0000-0002-3274-566X
Umberto Zanovello https://orcid.org/0000-0001-6415-9967
Luca Zilberti https://orcid.org/0000-0002-2382-4710

References

Arduino A, Bottauscio O, Brühl R, Chiampi M and Zilberti L 2019 In silico evaluation of the thermal stress induced by MRI switched gradient fields in patients with metallic hip implant *Phys. Med. Biol.* **64** 245006

Arduino A, Bottauscio O, Chiampi M and Zilberti L 2017 Douglas–Gunn method applied to dosimetric assessment in magnetic resonance imaging *IEEE Trans. Magn.* **53** 5000204

Arduino A, Zanovello U, Hand J, Zilberti L, Brühl R, Chiampi M and Bottauscio O 2021 Heating of hip joint implants in MRI: The combined effect of RF and switched-gradient fields *Magn. Reson. Med.* **85** 3447–62

ASTM F2182-19e2 2019 *Standard Test Method for Measurement of Radio Frequency Induced Heating on or Near Passive Implants During Magnetic Resonance Imaging* (West Conshohocken, PA, USA: ASTM International)
Bassen H and Zaidi T 2022 Parameters affecting worst-case gradient-field heating of passive conductive implants *J. Magn. Reason. Imag.* **56** 1197–204
Bhusal B *et al* 2021 Effect of device configuration and patient's Body composition on the RF heating and nonsusceptibility artifact of deep brain stimulation implants during MRI at 1.5T and 3T *J. Magn. Res. Imaging* **53** 599–610
Bottauscio O, Chiampi M, Hand J and Zilberti L 2015 A GPU Computational Code for Eddy-Current Problems in Voxel-Based Anatomy *IEEE Trans. Magn.* **51** 5100904
Chen J X, Wechsler H, Pullen J M, Zhu Y and MacMahon E B 2001 Knee surgery assistance: Patient model construction, motion simulation, and biomechanical visualization *IEEE Trans. Biomed. Eng.* **48** 1042–52
Destruel A *et al* 2019 A numerical and experimental study of RF shimming in the presence of hip prostheses using adaptive SAR at 3 T *Magn. Reson. Med.* **81** 3826–39
El-Bojairami I, El-Monajjed K and Driscoll M 2020 Development and validation of a timely and representative finite element human spine model for biomechanical simulations *Sci. Rep.* **10** 21519
Fiedler T M, Ladd M E and Bitz A K 2018 SAR simulations & safety *NeuroImage* **168** 33–58
Golestanirad L, Angelone L M, Iacono M I, Katnani H, Wald L and Bonmassar G 2017 Local SAR near deep brain stimulation (DBS) electrodes at 64 and 127 MHz: A simulation study of the effect of extracranial loops *Magn. Reson. Med.* **78** 1558–65
Gosselin M C *et al* 2014 Development of a new generation of high-resolution anatomical models for medical device evaluation: the Virtual Population 3.0 *Phys. Med. Biol.* **59** 5287–303
Guerin B *et al* 2018 Realistic modeling of deep brain stimulation implants for electromagnetic MRI safety studies *Phys. Med. Biol.* **63** 095015
Hasgall P A, Di Gennaro F, Baumgartner C, Neufeld E, Lloyd B, Gosselin M C, Payne D, Klingenböck A and Kuster N 2018 Version 4.1, Feb 22, 2022. IT'IS Database for thermal and electromagnetic parameters of biological tissues (https://doi.org/10.13099/VIP21000-04-1)
Iacono M I, Makris N, Mainardi L, Angelone M and Bonmassar G 2013 MRI-based multiscale model for electromagnetic analysis in the human head with implanted DBS *Comput. Math. Methods Med.* **2013** 694171
ISO_TS_10974_2018(E) Assessment of the safety of magnetic resonance imaging for patients with an active implantable medical device
Jeong H *et al* 2021 Development, validation, and pilot MRI safety study of a high-resolution, open source, whole body pediatric numerical simulation model *PLoS One* **16** e0241682
Madden J C, Enoch S J, Paini A and Cronin M T D 2020 A review of *in silico* tools as alternatives to animal testing: principles, resources and applications *Atla-Altern. Lab Animals* **48** 146–72
Mattei E *et al* 2008 Complexity of MRI induced heating on metallic leads: experimental measurements of 374 configurations *Biomed. Eng. Online* **7** 1–16
Mattei E, Calcagnini G, Censi F, Triventi M and Bartolini P 2010 Numerical model for estimating rf-induced heating on a pacemaker implant during MRI: Experimental validation *IEEE Trans. Biomed. Eng.* **57** 2045–52
McElcheran C E *et al* 2019 Numerical simulations of realistic lead trajectories and an experimental verification support the efficacy of parallel radiofrequency transmission to reduce heating of deep brain stimulation implants during MRI *Sci. Rep.* **9** 1–14
McElcheran C E, Yang B, Anderson K J T, Golenstani-Rad L and Graham S J 2015 Investigation of parallel radiofrequency transmission for the reduction of heating in long conductive leads in 3 tesla magnetic resonance imaging *PLoS One* **10** e0134379
Moghadam M N, Abdel-Sayed P, Camine V M and Pioletti D P 2015 Impact of synovial fluid flow on temperature regulation in knee cartilage *J. Biomech.* **48** 370–4
Nguyen B T *et al* 2022 Safety of MRI in patients with retained cardiac leads *Magn. Reson. Med.* **87** 2464–80
Nordbeck P *et al* 2009 Measuring RF-induced currents inside implants: impact of device configuration on MRI safety of cardiac pacemaker leads *Magn. Reson. Med.* **61** 570–8
OECD/EU 2016 *Health at a Glance: Europe 2016—State of Health in the EU Cycle* (Paris: OECD Publishing) (https://doi.org/10.1787/9789264265592-en). Accessed 14 June 2021
Powell J, Papadaki A, Hand J, Hart A and McRobbie D 2012 Numerical simulation of SAR induced around Co-Cr-Mo hip prostheses *in situ* exposed to RF fields associated with 1.5 and 3 T MRI body coils *Magn. Reson. Med.* **68** 960–8
Santoro D *et al* 2012 Detailing radio frequency heating induced by coronary stents: a 7.0 Tesla magnetic resonance study *PLoS One* **7** e49963
Seo Y and Wang Z J 2021 Measurement and evaluation of specific absorption rate and temperature elevation caused by an artificial hip joint during MRI scanning *Sci. Rep.* **11** 1–12
Sim4Life *Computable Human Phantoms* (Zurich: Zurich MedTech AG) (https://zmt.swiss/sim4life/)
Song T, Xu Z H, Iacono M I, Angelone L M and Rajan S 2018 Retrospective analysis of RF heating measurements of passive medical implants *Magn. Reson. Med.* **80** 2726–30
Viceconti M, Pappalardo F, Rodriguez B, Horner M, Bischoff J and Tshinanu F M 2021 In silico trials: verification, validation and uncertainty quantification of predictive models used in the regulatory evaluation of biomedical products *Methods* **185** 120–7
Winter L, Seifert F, Zilberti, Murbach M and Ittermann B 2021 Development of a new generation of high-resolution anatomical models for medical device evaluation: the Virtual Population 3.0 *J. Magn. Reson. Imag.* **53** 1646–65
Wolf S, Diehl D, Gebhardt M, Mallow J and Speck O 2013 SAR simulations for high- field MRI: how much detail, effort, and accuracy is needed ? *Magn. Reson. Med.* **69** 1157–68
Wooldridge J *et al* 2021 Gradient coil and radiofrequency induced heating of orthopaedic implants in MRI: influencing factors *Phys. Med. Biol.* **66** 245024
Yao A, Goren T, Samaras T, Kuster N and Kainz W 2021 Radiofrequency-induced heating of broken and abandoned implant leads during magnetic resonance examinations *Magn. Reson. Med.* **86** 2156–64
Zilberti L, Zanovello U, Arduino A, Bottauscio O and Chiampi M 2021 RF-induced heating of metallic implants simulated as PEC: is there something missing ? *Magn. Reson. Med.* **85** 583–6